Dalton Transactions

CfbA Promotes Insertion of Cobalt and Nickel into Ruffled Tetrapyrroles *in vitro*

Journal:	*Dalton Transactions*
Manuscript ID	DT-ART-09-2019-003601.R2
Article Type:	Paper
Date Submitted by the Author:	11-Dec-2019
Complete List of Authors:	Schuelke-Sanchez, Ariel; University of Vermont, Department of Chemistry Stone, Alissa; University of Vermont, Department of Chemistry Liptak, Matthew; University of Vermont, Department of Chemistry

PAPER

CfbA Promotes Insertion of Cobalt and Nickel into Ruffled Tetrapyrroles *in vitro*

Received 00th January 20xx,
Accepted 00th January 20xx

DOI: 10.1039/x0xx00000x

Ariel E. Schuelke-Sanchez,[a] Alissa A. Stone,[a] and Matthew D. Liptak*[a]

The nickel chelatase CfbA is the smallest member of the chelatase family, but the mechanism by which this enzyme inserts nickel into sirohydrochlorin is unknown. In order to gain mechanistic insight; metal binding, tetrapyrrole binding, and enzyme activity were characterized for a variety of substrates using several spectroscopic and computational approaches. Mass spectrometery and magnetic circular dichroism experiments revealed that CfbA binds an octahedral, high-spin metal substrate. UV/Vis absorption spectroscopy demonstrated that the enzyme binds a wide range of tetrapyrrole substrates and perturbs their electronic structures. Based upon activity assays, CfbA promotes insertion of cobalt and nickel into several tetrapyrroles, including cobalt insertion into protopophyrin IX. Finally, density functional theory models were developed which strongly suggest that observed spectral changes upon binding to the enzyme can be explained by tetrapyrrole ruffling, but not deprotonation or saddling. The observation of an octahedral, high-spin metal bound to CfbA leads to a generalization for all class II chelatases: these enzymes bind labile metal substrates and metal desolvation is not a rate-limiting step. The conclusion that CfbA ruffles its tetrapyrrole substrate reveals that the CfbA mechanism is different from that currently proposed for ferrochelatase, and identifies an intriguing correlation between metal substrate specificity and tetrapyrrole distortion mode in chelatases.

Introduction

Metal tetrapyrroles catalyse a myriad of important chemical transformations both in biological and abiological environments. A fundamental reason why metal tetrapyrroles can catalyse diverse chemistry is the incorporation of a transition metal that can access a larger number of reaction mechanisms than a main group element. In biological systems, the combination of iron and porphyrin, or heme, catalyses a variety of oxygen-dependent reactions,[1] including hydroxylation of alkanes,[2] degradation of peroxides to alcohols,[3] and reduction of molecular oxygen to water.[4] Vitamin B_{12} and cofactor F_{430} are cobalt and nickel tetrapyrroles, respectively, that catalyse methyl group transfer,[5] organic radical rearrangements,[6] and methanogenesis.[7] From an abiological perspective, metal tetrapyrroles have shown promise catalysing reactions critical for next-generation alternative energy applications, such as oxygen reduction,[8] hydrogen evolution,[8] and methane oxidation.[9] All of these transformations rely upon earth-abundant transition metals, so there is significant motivation to discover efficient routes to a broad range of metal tetrapyrroles.

In biological systems, a family of enzymes known as chelatases are involved in the biosynthesis of metal tetrapyrroles. *In vivo* each of these enzymes must catalyse the insertion of a specific metal into a specific tetrapyrrole ligand.[10] Chelatases have been divided into three classes.[11] Class I chelatases require ATP and are involved in the biosynthesis of chlorophyll and cobalamin.[12, 13] Class II chelatases do not require additional substrates beyond metal and tetrapyrrole. These enzymes either insert iron into protoporphyrin IX (PPIX),[14] or a 3*d* metal into the more reduced sirohydrochlroin (SHC) ring.[15-17] Finally, class III chelatases are multifunctional enzymes involved in siroheme biosynthesis.[18]

The smallest member of the chelatase family is CfbA (previously annotated as $CbiX^S$), and the enzymatic mechanism for this nickel chelatase has remained elusive. Elucidation of the CfbA mechanism is of particular importance because this enzyme is proposed to be the ancestor of all class II chelatases.[11] In support of this proposal, random in-frame mutagenesis of CfbA can produce synthetic proteins that resemble either the cobalt chelatase CbiK or the iron chelatase HemH.[19] With regards to the substrate scope of CfbA, this enzyme has been shown to insert iron,[11, 19] cobalt,[11, 19, 20] and nickel into SHC (Fig. 1).[11, 17, 21] Very little is known regarding the mechanism of CfbA. Based upon a structural overlay with CbiK, CfbA is proposed to bind a 3*d* metal via two His residues.[20] CfbA is also proposed to bind a distorted SHC based upon the crystal structure of product-bound enzyme.[22] We anticipate that insight into the CfbA mechanism will facilitate development of artificial chelatases that catalyse the formation of non-natural metal tetrapyrroles.

Metal and tetrapyrrole binding by CfbA, along with chelatase activity, for a diverse set of substrates has been

Department of Chemistry, University of Vermont, Burlington, Vermont 05405, USA. E-mail: matthew.liptak@uvm.edu

†Electronic Supplementary Information (ESI) available: DNA sequencing data, FPLC trace, SDS-PAGE gels, additional UV/Vis Abs spectra, and Cartesian coordinates. See DOI: 10.1039/x0xx00000x

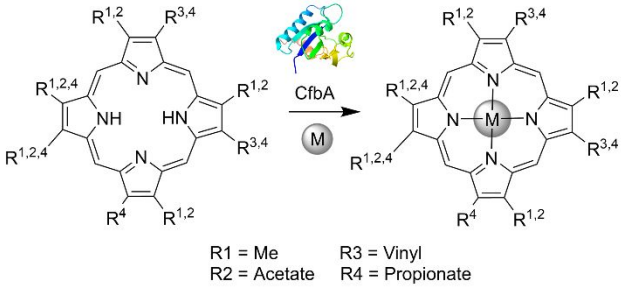

Fig. 1 Cobalt and nickel insertion into five porphyrin substrates by CfbA will be carefully assessed to gain insight into the enzymatic mechanism. The porphyrin substrates have different side-chain substitutions from one another.

assessed in order to elucidate the enzymatic mechanism. This approach is essential because some combinations of metal and tetrapyrrole can combine spontaneously resulting in misleading specific activity data.[17] Furthermore, binding of only one substrate (metal or tetrapyrrole) could promote insertion *in vitro*. This mechanism is exceedingly unlikely *in vivo* where metal and tetrapyrrole concentrations are regulated.[10, 17, 21] Metal binding by CfbA was measured with electrospray ionization mass spectrometry (ESI-MS) and magnetic circular dichroism (MCD) spectroscopy. Tetrapyrrole binding by CfbA was characterized using UV/Vis absorption (Abs) spectroscopy. Finally, chelatase activity for different combinations of metal and tetrapyrrole substrates was monitored using a combination of UV/Vis Abs spectroscopy and ESI-MS. By interpreting these data within the framework of density functional theory (DFT) and time-dependent DFT (TDDFT) calculations, we gained insight into the enzymatic mechanism of CfbA.

Experimental

Unless otherwise noted, we purchased all materials in this work from Fisher Scientific and used them without further purification.

Cloning, expression, and purification of CfbA

DNA plasmids encoding *Archaeoglobus fulgidus* CfbA, S219V tobacco etch virus (TEV) protease, and *Staphylococcus aureus* IsdG were obtained. We designed a synthetic gene encoding CfbA that was optimized for *Escherichia coli* codon usage. Integrated DNA Technologies (Coralville, IA) synthesized this *cfbA* gene and inserted it into pIDTSMART (Kan^r). Eric Skaar (Vanderbilt University) gifted a pET15b (Amp^r, Novagen) plasmid encoding IsdG.[23] Lastly, David Waugh (National Cancer Institute) provided a pRK793 (Amp^r) plasmid encoding S219V TEV protease.[24, 25]

A pET15b vector encoding CfbA with a TEV-cleavable N-terminal His_6 tag was prepared. The SalI and BamHI restriction enzymes (New England Biolabs) were used to digest the pIDTSMART plasmid encoding CfbA and the pET15b plasmid encoding IsdG. Next, the cfbA and pET15b DNA fragments were isolated via gel electrophoresis and recovered using the QIAquick gel extraction kit (Qiagen). The cfbA gene was ligated to pET15b by overnight incubation with T4 DNA ligase (New England Biolabs) followed by purification using a QIAprep spin mini-prep kit (Qiagen). DNA sequencing by the Vermont Cancer Center DNA analysis facility confirmed the sequence of the resulting CfbA-encoding pET15b (Amp^r) vector (Table S1).

Recombinant CfbA and S219V TEV protease were overexpressed in BL21-GOLD(DE3) cells (Strategene). BL21-GOLD(DE3) cells containing the CfbA-encoding pET15b (Amp^r) vector were grown at 37 °C in Luria-Bertani (LB) medium containing 100 µg ampicillin using a ThermoScientific MaxQ incubator shaker, which is similar to a previously reported procedure.[20] CfbA expression was induced at an OD_{600} of 0.6 a.u. by the addition of isopropyl-β-D-1-thiogalactopyranoside (IPTG), followed by growth at 30 °C for at least five hours. These cells were harvested by centrifugation at 10,000 x *g* and 4 °C for 10 minutes using a ThermoScientific Sorvall Legend centrifuge. The second enzyme used in this work, S219V TEV protease, was expressed and purified as previously described.[24, 25]

N-terminal His_6-tagged CfbA was purified using affinity chromatography. Cell pellets containing overexpressed CfbA were resuspended in 50 mM 4-(2-hydroxyethyl)-1-piperazineethanesulfonic acid (HEPES) pH 7.5 with 500 mM NaCl, 5 mM imidazole, and 5% glycerol (*v*/*v*). Enough phenylmethanesulfonyl fluoride and lysozyme were added to this suspension to reach final concentrations of 1.0 mM and 0.5 mg/mL, respectively, prior to sonication. A Branson Ultasonics sonifier lysed the resuspended cells to release overexpressed CfbA from the *E. coli* cells. The resulting lysate was clarified by centrifugation at 15,000 x *g* and 4 °C followed by vacuum filtration with a 0.45 µm membrane (Millipore). The clarified lysate was loaded onto a nickel HiTrap HP 5 mL column (GE Healthcare) equilibrated with 50 mM HEPES pH 7.5, 500 mM NaCl, 5 mM imidazole, and 5% glycerol (*v*/*v*) using an Äkta pure chromatography system (GE Healthcare). The loaded column was washed with an imidazole gradient from 5 to 500 mM over 200 mL. Pure, N-terminal His_6-tagged CfbA eluted at 500 mM imidazole (Fig. S1).

The N-terminal His_6 tag was removed from purified CfbA using S219V TEV protease. S219V TEV protease was added to His_6-tagged CfbA in an A_{280} ratio of 3:100 with sufficient dithiothreitol and ethylenediaminetetraacetic acid to reach final concentrations of 1 mM and 0.5 mM, respectively.[25] The solution was dialyzed twice against 10 mM HEPES pH 7.5, 500 mM NaCl at 4 °C for three hours each. After increasing the imidazole concentration to 75 mM, the dialyzed solution was loaded onto a HisPur Co-NTA gravity column equilibrated with 50 mM HEPES pH 7.5, 500 mM NaCl, 5 mM imidazole, and 5% glycerol (*v*/*v*). Following protein loading, the column was washed with 50 mM HEPES pH 7.5, 500 mM NaCl, 75 mM imidazole, and 5% glycerol (*v*/*v*) to elute pure, untagged CfbA (Fig. S2). The flow-throughs from the loading and wash steps containing pure, untagged CfbA were combined and the volume was reduced to 10 mL using Amicon stirred cell ultrafiltration cells (Millipore). The concentrated CfbA solution was dialyzed twice against 10 mM HEPES pH 7.5, 500 mM NaCl at 4 °C for three hours each yielding pure, cleaved CfbA. CfbA was >99% pure according to SDS-PAGE gel electrophoresis (Fig. S3). Based

upon a Bradford assay using bovine serum albumin (Pierce) as the standard, the CfbA yield was 30 mg per 1 L of LB medium.

CfbA characterization

The molecular weight of pure, untagged CfbA was determined using ESI-MS. 143 μM CfbA in 10 mM HEPES pH 7.5, 500 mM NaCl was prepared. This sample was loaded onto a C_{18} guard column equilibrated with 2% acetonitrile with 0.1 % formic acid (*v*/*v*) in water (*v*/*v*). A gradient from 2% to 98% acetonitrile was used to separate CfbA prior to ESI-MS analysis using an AB-Sciex 4000 Q Trap LCMS/MS spectrometer (Applied Biosystems). ESI-MS data for 600-1700 m/z was acquired in positive ion mode and deconvoluted using BioAnalyst 1.5.

The secondary structure of CfbA was assessed using circular dichroism (CD) spectroscopy. A 10 μM CfbA sample was exchanged into 10 mM potassium phosphate (KP_i) pH 7.5 using a PD-10 column (GE Healthcare) and loaded into a 1 mm path length quartz cuvette (Starna). The CD spectrum was collected from 250 to 190 nm with a scan rate of 200 nm/min and a 0.5 nm data interval on a Jasco J-815 CD spectrometer. The secondary structure was estimated from the resulting data using the PLS method in the CD multivariate SSE program (Jasco).

Metal binding

Metal binding by CfbA was evaluated using ESI-MS. Stock solutions of 20 mM Co(II) or Ni(II) in 50 mM Tris pH 8.0, 150 mM NaCl were prepared by adding sufficient $CoCl_2$ or $NiSO_4$, respectively, to aqueous buffer. Next, the Co(II) or Ni(II) solution was combined with purified CfbA yielding 5 μM CfbA in 50 mM Tris pH 8.0, 150 mM NaCl, 200 μM $CoCl_2$ or $NiSO_4$. CfbA was loaded onto a C_4 column equilibrated with 2% acetonitrile with 0.1 % formic acid (*v*/*v*) in water (*v*/*v*). The same ESI-MS protocol described above for apoprotein characterization was employed for the metal-loaded CfbA samples. The resulting data was deconvoluted with the BioAnalyst 1.5 software program.

The metal coordination site was characterized using MCD spectroscopy. Sufficient $CoCl_2$ and glycerol were added to purified, concentrated CfbA to yield 400 μM CfbA in 50 mM KP_i pH 8.0, 50 mM NaCl, 400 μM $CoCl_2$, and 60% glycerol (*v*/*v*). In addition, a sample of 400 μM $CoCl_2$ in the same aqueous buffer was prepared. These two samples were loaded into copper/quartz sample cells and flash frozen in liquid nitrogen. The samples were equilibrated at temperatures of 2, 5, 10, and 20 K along with magnetic fields of ±1, 3, 5, and 7 T using an Oxford SM4000-8T Spectromag. MCD data between 800 and 300 nm were acquired under these conditions using a Jasco J-815 CD spectrometer with a scanning speed of 200 nm/min, a bandwidth of 1 nm, a digital integration time of 0.25 s, and a data pitch of 0.5 nm. For all MCD data, the negative magnetic field spectrum was subtracted from the positive field data and the result was divided by 2 to remove the CD contribution.

Tetrapyrrole binding

Tetrapyrrole binding by CfbA was assessed using UV/Vis Abs spectroscopy. Uroporphyrin I, uroporphyrin III, coproporphyrin I, and coproporphyrin III were purchased from Frontier Scientific and dissolved in 50 mM Tris pH 8.0, 150 mM NaCl. Protoporphyrin IX was also purchased from Frontier Scientific, but dissolved in methanol prior to preparation of a solution sample in 50 mM Tris pH 8.0, 150 mM NaCl, and 10 % (*v*/*v*) methanol. These tetrapyrrole solutions were diluted to 6 μM based upon reported extinction coefficients,[26-30] wrapped in aluminium foil to prevent photodegradation, and used the same day as preparation to mitigate aggregation (Fig. S4). CfbA-bound tetrapyrrole samples were prepared by combining tetrapyrrole and CfbA solutions in a 1:1 molar ratio. UV/Vis Abs spectra in the 800-350 nm region were recorded for protein-free and CfbA-bound tetrapyrroles using a Cary 100 Bio spectrophotometer with a scan rate of 600 nm/min, a bandwidth of 2 nm, an averaging time of 0.1 s, and a 0.5 nm data interval.

Activity assays

The rates of metal insertion into uroporphyrin and coproporphyrin by CfbA were quantified using UV/Vis Abs spectroscopy. The rates of cobalt and nickel insertion in the presence of CfbA were measured in aqueous solution with 5-6 μM CfbA and tetrapyrrole along with either 200 μM $CoCl_2$ or 200 μM $NiSO_4$ in 50 mM Tris pH 8.0 with 150 mM NaCl. The rates of metal insertion in the absence of CfbA were measured in nearly identical solutions that lacked enzyme. In order to monitor the formation of metal tetrapyrrole, UV/Vis Abs spectra were acquired using the same instrument and parameters as described above. For metal insertion into the uroporphyrins, and cobalt insertion into the coproporphyrins, new UV/Vis spectra were acquired every minute for a total of 0.5-30 h. For nickel insertion into the coproporphyrins, new spectra were acquired every hour for 30-72 h. The assays were performed in triplicate. The pseudo-first order rate constants, and their standard deviations, for CfbA-promoted and enzyme-free metal insertion into uroporphyrin and coproporphyrin were determined by fitting the data to equation 1 with Graph Pad Prism.

$$A = (A_0 - B)e^{-kx} + B \quad (1)$$

Where A is the absorbance intensity, A_0 is the absorbance at time(x) equal to zero, B is the absorbance intensity at infinite time, and k is the rate constant.

Metal insertion into protoporphyrin IX by CfbA was characterized with UV/Vis Abs spectroscopy and ESI-MS. 200 μM cobalt insertion into 5 μM protoporphyrin IX, both in the presence and absence of 5 μM CfbA, was monitored every 15 minutes in 50 mM Tris pH 8.0, 150 mM NaCl, and 10 % methanol (*v*/*v*) for 18 hours by UV/Vis spectroscopy. Similarly, 200 μM nickel insertion into 5 μM protoporphyrin IX, both in the presence and absence of 5 μM CfbA, was monitored every hour for 72 hours. In addition, 300-1500 m/z ESI-MS data for cobalt insertion reactions were acquired after 72 hours using a C_{18} guard column using the same instrument, solvent gradient, and analysis software described above. In order to identify the binding and oxidation state of the reaction product, Co(III) protoporphyrin IX was purchased from Frontier Scientific and

dissolved in 50 mM Tris pH 8.0, 150 mM NaCl, and 10 % methanol (*v*/*v*). A Co(II) protoporphyrin IX solution was prepared by reducing a deoxygenated Co(III) protoporphyrin IX solution with excess sodium dithionite under anaerobic conditions. A 10 µM Co(III) protoporphyrin IX solution was prepared based upon a published extinction coefficient,[31] half of the solution was combined with 10 µM CfbA, and UV/Vis spectra were acquired after 18 hours. Finally, an anaerobic 10 µM Co(II) protoporphyrin IX solution was prepared, half of that solution was combined with deoxygenated 10 µM CfbA under anaerobic conditions, and UV/Vis spectra of these two samples were acquired using screw top cuvettes (Starna).

Computational characterization

DFT models of octamethylporphyrin and doubly deprotonated octamethylporphyrin were prepared to aid interpretation of the experimental data. The initial structural model was generated in ChemDraw (PerkinElmer), and hydrogen atoms were added in ArgusLab (Planaria Software). All electronic structure calculations were performed in the ORCA 4.0.0.2 software package on the Bluemoon cluster of the Vermont Advanced Computing Core.[32] Geometry optimizations were completed using the BLYP,[33, 34] B3LYP,[35] PBE,[36] and PBE0[37] density functionals in combination with a def2-TZVP basis set,[38] very tight SCF convergence criteria, and an implicit solvation model. The conductor-like polarizable continuum model (CPCM) was used to model the influence of methanol solvation on the geometric and electronic structure of octamethylporphyrin and its dianion.[39] For each optimized DFT model, vibrational frequency calculations were performed to ascertain whether the structure represented a true minimum on the potential energy surface.

TDDFT was employed to predict the UV/Vis Abs spectra of octamethylporphryin and its dianion. These calculations utilized the same density functionals, basis set, and solvation model described above for geometry optimizations. The TDDFT calculations predicted the first 30 electronic states using an expansion space of up to six vectors per root. Finally, the UV/Vis Abs spectra were simulated based upon the TDDFT data by convoluting Gaussian-shaped bands with full width at half-maximum bandwidths of 1500 cm^{-1}.

The ground- and excited-state potential energy surfaces along the lowest energy ruffling and saddling normal modes were computed. Geometric coordinates for distortions along <100 cm^{-1} vibrational modes for the BLYP/def2-TZVP model of octamethylporphyrin described above were extracted using gOpenMol.[40, 41] These coordinates were analysed by the normal-coordinate structural decomposition program to identify and categorize out-of-plane deformation modes.[42, 43] The b_{1u} ruffling distortion was found to be a 42.6 cm^{-1} mode and the b_{2u} saddling distortion was identified as a 22.2 cm^{-1} vibration. The ground- and excited-state potential energy surfaces along these two modes were predicted using the MTR subprogram of ORCA. For each mode, 50 dimensionless normal-coordinate displacements of 0.05 a.u. in both the positive and negative directions from the equilibrium geometry were computed.

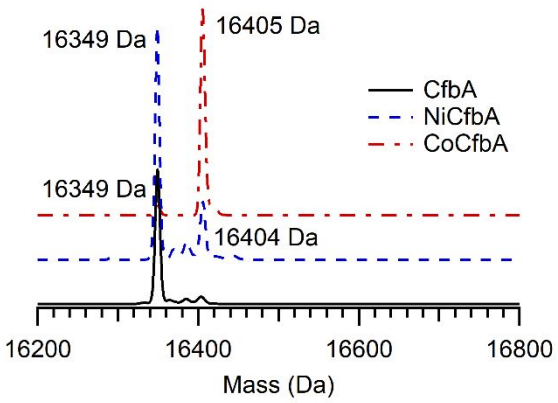

Fig. 2 ESI-MS spectra of CfbA (black line), nickel-bound CfbA (NiCfbA, dashed blue line), and cobalt-bound CfbA (CoCfbA, dashed red line). The observed masses of CfbA (16349 Da), NiCfbA (16404 Da), and CoCfbA (16405 Da) are consistent with the formation of a 1:1 complex between CfbA and a metal substrate.

Results

Recombinant CfbA is properly folded

ESI-MS and CD data confirmed that the recombinant CfbA characterized in this work is identical to the native enzyme. The molecular weight of purified, recombinant CfbA is 16,349 Da according to ESI-MS (Fig. 2). Considering experimental error, this is consistent with the expected isotopically averaged mass of 16,347 Da for monomeric CfbA. Next, the secondary structure of CfbA was estimated using CD spectroscopy. The secondary structure of CfbA in solution is estimated to be 29 ± 1 % α-helix and 19 ± 1 % β-sheet based upon analysis of the CD spectrum (Fig. S5). This secondary structure is similar to that observed in the X-ray crystal structure of monomeric *A. fulgidus* CfbA (PDB ID 1TJN, 28 % α-helix and 18 % β-sheet).[20] The CD spectrum is less consistent with the dimeric X-ray crystal structure (PDB ID 2DJ5, 32 % α-helix and 21 % β-sheet). Thus, CfbA is likely a monomeric protein with a solution structure similar to its monomeric solid-state structure.

CfbA binds cobalt or nickel at an octahedral site

ESI-MS data demonstrate metal binding to CfbA. The molecular weights of CfbA following incubation with 40-fold molar excesses of $CoCl_2$ or $NiSO_4$ are 16,405 Da and 16,404 Da, respectively (Fig. 2). The most abundant isotopes of cobalt and nickel have molecular weights of 59 and 58 Da, respectively, so these mass changes are consistent with binding a single metal ion considering experimental error. Alternatively, the 1 Da discrepancy between the expected and observed masses could be due to deprotonation of a single amino acid, such as histidine, upon metal binding. Based upon ESI-MS intensities, CfbA is almost fully cobalt-bound and about 10% nickel-bound under the conditions employed here. Thus, further

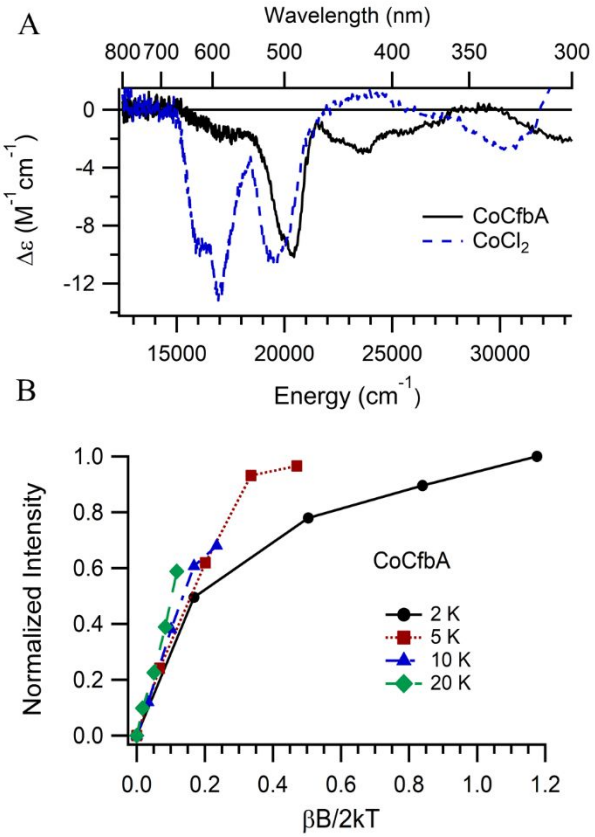

Fig. 3 5 K, 7 T MCD spectra of $CoCl_2$ (blue, dashed) and CoCfbA (black) in 50 mM KPi pH 8.0, 50 mM NaCl, 60 % (*v*/*v*) glycerol (A). 2, 5, 10, and 20 K saturation magnetization curves for the 495 nm band of CoCfbA constructed from MCD data acquired at 0, 1, 3, 5, and 7 T (B). The $CoCl_2$ spectrum is consistent with a five-coordinate species, and the CoCfbA MCD data indicate the presence of a six-coordinate, *S* = 3/2 Co(II) ion.

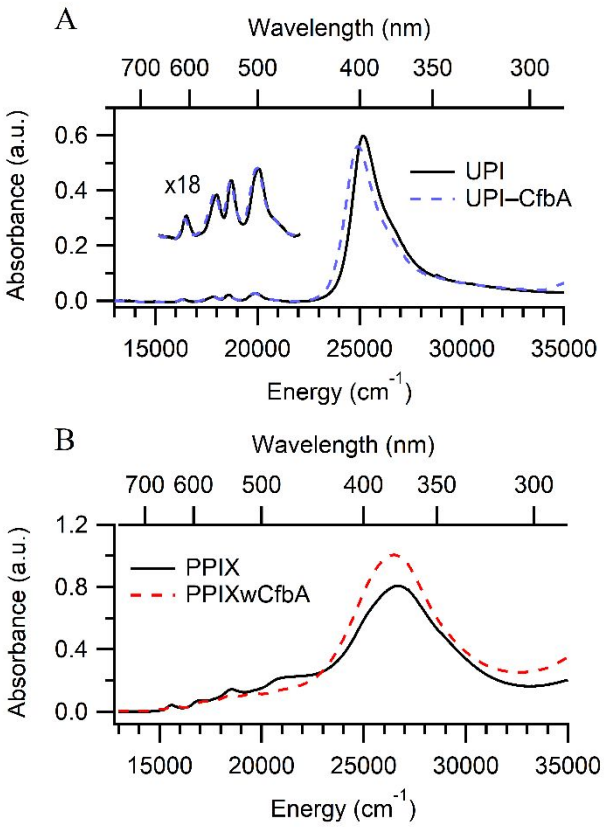

Fig. 4 UV/Vis Abs spectra of 6 µM UPI in 50 mM Tris pH 8.0 and 150 mM NaCl, both in the absence (solid black line) and presence (dashed blue line) of equimolar CfbA (A). UV/Vis Abs spectra of 6 µM PPIX in 50 mM Tris pH 8.0, 150 mM NaCl, and 10% (*v*/*v*) methanol without (solid black line) and with (dashed red line) equimolar CfbA (B). CfbA binding perturbs the electronic structures of both porphyrins.

spectroscopic characterization of metal binding by CfbA focused on cobalt-bound CfbA.

MCD spectroscopy revealed that CfbA-bound cobalt is an octahedral, high-spin Co(II) species. The MCD spectrum of CfbA-bound cobalt is dominated by a temperature-dependent, negatively-signed band at 495 nm (Fig. 3A). This is consistent with an octahedral Co(II) complex lacking cysteine ligands, where one or more of the ligands may be solvent-derived.[44, 45] In contrast, the MCD spectrum of $CoCl_2$ in the absence of CfbA has three negatively-signed bands at 623, 590, and 511 nm. These data indicated that aqueous Co(II) is five-coordinate in the 50 mM KP_i pH 8.0, 50 mM NaCl, and 60 % glycerol (*v*/*v*) buffer used for MCD studies (Fig. S6).[46] In order to determine the spin-state of CfbA-bound Co(II), the intensity of the 495 nm MCD band was plotted as a function of sample temperature and applied magnetic field (Fig. 3B). The "nesting" of the isotemperature curves is unambiguous evidence for a high-spin (*S* = 3/2) Co(II) ion.[47] Thus, CfbA binds high-spin Co(II) with an octahedral coordination site comprised of nitrogen- and/or oxygen-based ligands.

CfbA binds a diverse set of tetrapyrroles

UV/Vis Abs data indicate that all five isomers of coproporphyrin, uroporphyrin, and protoporphyrin used in this study bind to CfbA. Upon binding to CfbA, the Soret bands of coproporphyrin I, uroporphyrin I, and uroporphyrin III decrease in intensity and broaden (Fig. 4A, S7). These changes are most consistent with increased conformational heterogeneity for coproporphyrin I, uroporphyrin I, and uroporphyrin III upon binding to CfbA. On the other hand, the coproporphyrin III Soret band intensity increases upon binding to CfbA. This suggests that coproporphyrin III may adopt a more well-defined structure upon binding to the enzyme (Table S2). Similarly, the Soret band intensity of PPIX significantly increases upon binding to CfbA (Fig. 4B). In this case, the tetrapyrrole is only sparingly soluble in aqueous solution and its ill-advised to interpret the spectral changes as evidence for anything more than protein binding. Nevertheless, the UV/Vis Abs data do indicate that all five tetrapyrroles bind to CfbA and this event increases the conformational heterogeneity of coproporphyrin I, uroporphyrin I, and uroporphyrin III.

Binding to CfbA significantly shifts the energy of the Soret band, and introduces smaller perturbations to the Q band energies, for all five tetrapyrroles. The Soret band of coproporphyin I exhibits the largest red-shift of 1,100 cm^{-1} from 26,900 cm^{-1} to 25,800 cm^{-1} upon binding to CfbA (Table 1). Somewhat surprisingly, the other isomer of coproporphyrin studied here, copropophyrin III, undergoes a 400 cm^{-1} blue-shift upon binding to CfbA. The Soret bands of both uroporphyrin

Table 1 Soret band shifts for porphyrin substrates upon binding to CfbA

Porphyrin	Free (cm^{-1})	CfbA-bound (cm^{-1})	Bandshift (cm^{-1})
CPI	26,900	25,800	-1,100
CPIII	25,800	26,200	+400
UPI	25,200	24,900	-300
UPIII	25,200	24,800	-400
PPIX	26,700	26,300	-400

isomers and PPIX all moderately red-shift by 300-400 cm^{-1} upon binding to CfbA. On the other hand, the Q band components in the 15,000 to 21,000 cm^{-1} region do not consistently red- or blue-shift upon tetrapyrrole binding to CfbA. In the cases of coproporphyrin I and uroporphyrin I, CfbA binding does not induce any Q-band shifts that are larger than experimental error. For the other three tetrapyrroles, some Q-band components red- or blue-shift, but in none of these cases do all four Q-band components consistently red- or blue-shift (Table S3). Thus, the Soret band energies appear to be a useful spectroscopic probe for CfbA binding, but the Q band energies do not.

CfbA promotes metal insertion into several tetrapyrroles

CfbA increases the rate of cobalt insertion into coproporphyrin I, uroporphyrin I, and uroporphyrin III. Most notably, 5 µM uroporphyrin I was fully converted to cobalt-uroporphyrin I in under one minute by 5 µM CfbA in 50 mM Tris pH 8.0, 150 mM NaCl, and 200 µM $CoCl_2$ at room temperature (Fig. 5A). This represents a significant rate increase compared to the enzyme-free reaction, which converted 5 µM uroporphyrin I to cobalt-uroporphyrin I with a pseudo-first order rate constant of 0.095 ± 0.003 min^{-1} (Table 2). CfbA also promoted the insertion of cobalt into coproporphyrin I and uroporphyrin III. In these cases, the enzyme-promoted rates were 2.8- and 4.2-fold greater than the CfbA-free reactions, respectively. In contrast, the rate of cobalt insertion into coproporphyrin III was unchanged by the addition of CfbA (Fig. S8). Nevertheless, these data do clearly indicate that CfbA promotes cobalt insertion into three of the four isomers of coproporphyrin and uroporphyrin investigated here.

CfbA also promotes the insertion of cobalt into PPIX. Over the course of 72 hours in 50 mM Tris pH 8.0, 150 mM NaCl, and 10% methanol (*v*/*v*), CfbA converts $CoCl_2$ and PPIX to a product with an intense UV/Vis Abs maximum of 424 nm (Fig. 5B). Under these same conditions, but in the absence of CfbA, there is no observable product formation and instead PPIX partially precipitates out of solution.[48] ESI-MS was employed to assess whether the product with an intense 424 nm UV/Vis Abs maximum was CoPPIX (Fig. S9). Indeed, the reaction generates a product with a mass of 619.5 Da, which is consistent with formation of CoPPIX. Finally, samples of Co(III)PPIX and Co(II)PPIX were prepared non-enzymatically and characterized using UV/Vis Abs spectroscopy to determine the oxidation state of the enzyme product (Fig. S10). Based upon the results of these experiments, CfbA converts $CoCl_2$ and PPIX to enzyme-bound Co(III)PPIX.[31] Thus, formation of CfbA-bound Co(III)PPIX from Co(II) and PPIX is likely a two-step reaction where the

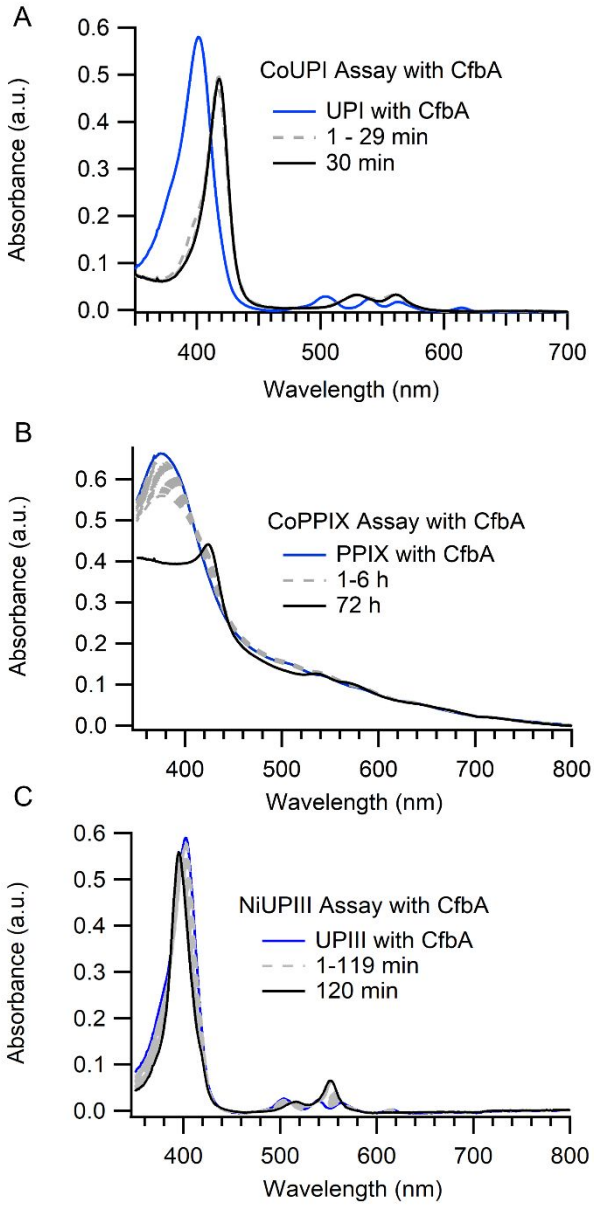

Fig. 5 UV/Vis Abs spectra of CfbA, UPI, and excess $CoCl_2$ in 50 mM Tris pH 8.0, 150 mM NaCl immediately following mixing (blue line), after 1-29 min. (dashed grey lines), and after 30 min (black line, A). UV/Vis Abs spectra of CfbA, PPIX, and excess $CoCl_2$ in 50 mM Tris pH 8.0, 150 mM NaCl, 10% methanol (*v*/*v*) immediately following mixing (blue line), after 1-6 h (dashed grey lines), and after 72 h (black line, B). UV/Vis Abs spectra of CfbA, UPIII, and excess $NiSO_4$ in 50 mM Tris pH 8.0, 150 mM NaCl immediately following mixing (blue line), after 1-119 min. (dashed grey lines), and after 120 min (black line, C). CfbA promotes conversion of UPI and PPIX to Co–UPI and Co–PPIX, respectively. CfbA also promotes conversion of UPIII to Ni–UPIII.

initial Co(II)PPIX product is rapidly oxidized by molecular oxygen following metal insertion.

Finally, CfbA also promotes nickel insertion into uroporphyrins I and III. Enzyme activity assays were carried out and analysed as described above for cobalt, only with nickel as the metal substrate. In the presence of 5 µM CfbA, 5 µM uroporphyrin III was converted to nickel-uroporphyrin III in 50 mM Tris pH 8.0, 150 mM NaCl, and 200 µM $NiSO_4$ over the course of two hours at room temperature (Fig. 5C). CfbA-

Table 2 Pseudo-first order rates for Co insertion into porphyrin substrates (min^{-1})

Porphyrin	Without CfbA	With CfbA	% Increase
CPI	0.0273 ± 0.0005	0.077 ± 0.002	180%
CPIII	0.078 ± 0.009	0.0796 ± 0.0003	2%
UPI	0.095 ± 0.003	>>1	>>900%
UPIII	0.110 ± 0.002	0.46 ± 0.02	320%
PPIX	0	>0	∞

Table 3 Pseudo-first order rates for Ni insertion into porphyrin substrates (min^{-1})

Porphyrin	Without CfbA	With CfbA	% Increase
CPI	0	0	0%
CPIII	0	0	0%
UPI	0	0.0029 ± 0.0002	∞
UPIII	0	0.0171 ± 0.0002	∞
PPIX	0	0	0%

catalysed Ni(II) insertion into uroporphyrin I was six-fold slower under these same conditions (Table 3). Unlike the Co(II) insertion assays, no Ni(II) insertion into either uroporphyrin was observed in the absence of CfbA (Fig. S11). As for the coproporphyrin and protoporphyrin substrates, nickel insertion was not observed in either the presence or absence of CfbA. Nevertheless, the data for coproporphyrin III merits further comment. Over the course of 30 hours, the Soret band for coproporphyrin III shifted from 389 to 403 nm in the presence of CfbA. However, the conversion of the Q band from four components to two components as is typically associated with tetrpyrrole metalation did not occur.[49, 50] Thus, we conclude that coproporphyrin III binds to CfbA, but Ni(II) is not inserted. To summarize the nickel activity assay data, CfbA catalyses nickel insertion into uroporphryins and Ni(II) insertion into uroporphyrin III is six times faster than insertion into uroporphyrin I.

CfbA ruffles uroporphyrin and protoporphyrin

A DFT model was developed in order to gain further insight into how CfbA promotes metal chelation. Due to the complex electronic structure of the porphyrin π system, it is necessary to validate potential DFT models using experimental UV/Vis Abs data prior to analysis. Thus, we developed fully geometry optimized models of octamethylporphyrin using the BLYP, PBE, B3LYP, and PBE0 density functionals (Fig. S12). The BLYP and PBE TDDFT-predicted Soret band energies are more similar to experiment than those predicted by TDDFT calculations with the B3LYP or PBE0 functionals, which indicates that the generalized gradient approximation functionals produce more accurate models of the porphyrin valence orbital energies and the configuration interaction mixing between the first two excited states.[49] The BLYP TDDFT calculation generates the most accurate Soret to Q band intensity ratio, which means that this is the most accurate model for valence orbital energies and configuration interaction mixing. However, the BLYP TDDFT-predicted Q-band region only exhibited three bands compared to the four observed experimentally. This is not necessarily surprising because the TDDFT model has neglected vibronic coupling,[50] and a wide range of theoretical models have failed

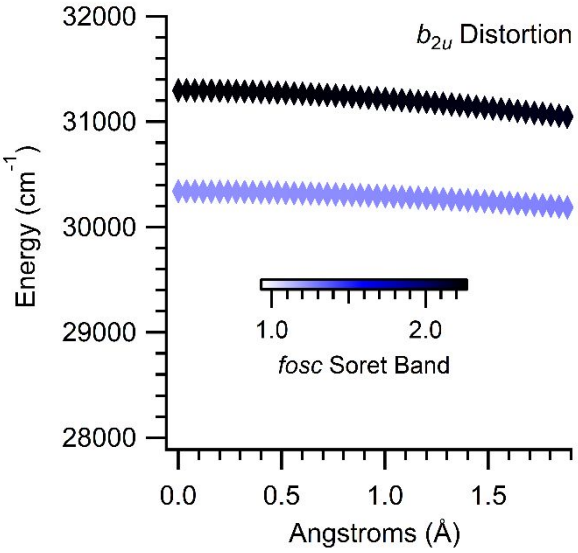

Fig. 6 BLYP TDDFT-predicted influence of a b_{2u} out-of-plane saddling deformation on the Soret band transition energies. Two TDDFT transitions (black and blue diamonds) contribute to the observed UV/Vis Abs band. The model predicts a 10-25 cm^{-1} red-shift of the Soret band per 0.1 Å of saddling from the equilibrium value of 0.15 Å. Porphyrin saddling cannot explain the porphyrin Soret bandshifts observed upon binding to CfbA.

to accurately reproduce this aspect of the porphyrin UV/Vis Abs spectrum.[51] Thus, the BLYP model will be used to elucidate CfbA-induced perturbations of the tetrapyrrole substrate, and our analysis will emphasize changes observed for the Soret band.

The BLYP model developed in this work reveals that the CfbA-induced changes to the tetrapyrrole UV/Vis Abs spectra do not arise from substrate deprotonation. This is an important discovery because small molecule studies have shown that porphyrin deprotonation does induce a red-shift of the Soret band as seen here for four of the five tetrapyrrole substrates upon binding to CfbA.[52] Furthermore, small molecule studies have shown that porphyrin deprotonation promotes metal chelation by generating four pyrrole nitrogen lone pairs.[53] Deprotonation of the BLYP model for octamethylporphyrin followed by geometry optimization and TDDFT prediction of the UV/Vis Abs spectrum does predict an 1,800 cm^{-1} red-shift of the Soret band (Fig. S13). However, the TDDFT calculations also predict a decrease in the number of Q bands to two, which has been observed previously for porphyrin structural changes that increase molecular symmetry.[50] The TDDFT-predicted red-shift of the Soret band upon porphyrin deprotonation is larger than any of the band-shifts observed in this study. Also, no significant changes to the shape of the Q-band region were observed experimentally for any of the five tetrapyrroles. Thus, we conclude that the CfbA-induced changes to the tetrapyrrole UV/Vis Abs spectra are not due to substrate deprotonation and must arise from a different structural change.

The DFT model developed here also reveals that the UV/Vis Abs changes observed upon binding substrate to CfbA cannot be attributed to a saddling deformation of the tetrapyrrole. The saddling deformation has been previously correlated with ferrochelatase activity,[54-57] and this distortion could explain the

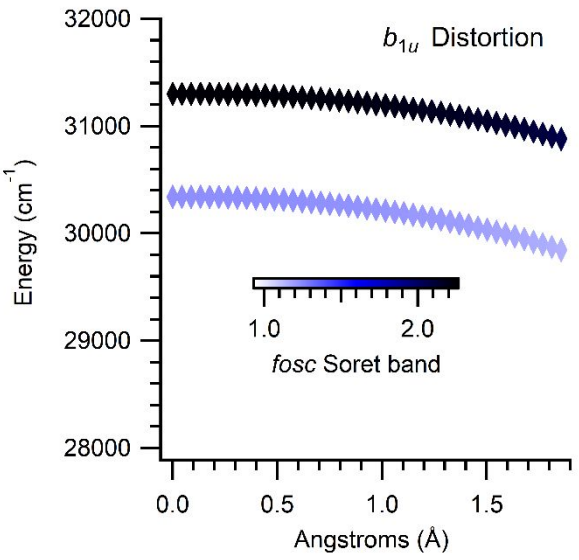

Fig. 7 BLYP TDDFT-predicted influence of a b_{1u} out-of-plane ruffling deformation on the Soret band transition energies. Two TDDFT transitions (black and blue diamonds) contribute to the observed UV/Vis Abs band. The model predicts a 20-100 cm^{-1} red-shift of the Soret band per 0.1 Å of ruffling from the equilibrium value of 0.12 Å. An increase of porphyrin ruffling to 1.4, 1.6, and 1.6 Å, respectively, can explain the UPI, UPIII, and PPIX Soret band red-shifts observed upon binding to CfbA.

disorder observed in the X-ray crystal structure of CfbA-bound metal sirohydrochlorin (PDB ID 2XWQ).[22] Thus, the computational model of octamethylporphyrin was distorted along its lowest energy saddling normal mode and the UV/Vis Abs spectrum was predicted by TDDFT at each point (Fig. 6). These calculations revealed that saddling induces a minor red-shift of the Soret band by 10-25 cm^{-1} per 0.1 Å for small distortions from the equilibrium value of 0.15 Å. This minor red-shift is consistent with previous computational studies which concluded that saddling does not significantly red-shift the tetrapyrrole Soret band.[58, 59] Due to the minor dependence of the Soret band energy on saddling, the 300-1,100 cm^{-1} red-shifts for coproporphyrin I, uroporphyrin, and PPIX could only be explained by saddling if CfbA-binding increases tetrapyrrole saddling to greater than 1.9 Å. In addition, the 400 cm^{-1} blue-shift of the coproporphyrin III Soret band could only be explained by saddling if CfbA-binding decreases the magnitude of this deformation to less than 0 Å! Since none of these large structural changes are consistent with the X-ray crystal structure of CfbA-bound metal sirohydrochlorin (PDB ID 2XWQ), we conclude that saddling is not the origin of the UV/Vis Abs changes observed here.

Instead of deprotonation or saddling, the computational model developed here identifies ruffling as the most likely origin of the CfbA-induced spectral changes. A series of TDDFT-predicted UV/Vis Abs spectra as a function of distortion along the lowest energy ruffling mode were generated (Fig. 7). These data predict that the tetrapyrrole Soret band will moderately red-shift by 20-100 cm^{-1} per 0.1 Å with increased ruffling from the equilibrium value of 0.12 Å. Even with this moderate dependence upon ruffling, the large Soret band shifts observed for CPI and CPIII upon binding to CfbA cannot be readily explained. Most likely, CfbA distorts coproporphyrin in a different fashion. However, the CfbA-induced 300-400 cm^{-1} red-shifts of the uroporphyrin and PPIX Soret bands are fully consistent with a ruffling deformation. Based upon the spectro-structural model described in this work, CfbA increases uroporphyrin I, uroporphyrin III, and PPIX ruffling to 1.4. 1.6, and 1.6 Å, respectively. Thus, while the CfbA-induced Soret band red-shifts for uroporphyrin and PPIX are too small to be attributed to pyrrole deprotonation, and too large to be attributed to a saddling deformation, but "just right" for enzyme-induced ruffling of the tetrapyrrole substrate.

Discussion

Class II chelatases bind labile transition metals

The MCD data presented in this work reveals that a labile metal binding site appears to be common to class II chelatases. Specifically, the MCD data clearly demonstrates that CfbA-bound cobalt is an octahedral, high-spin Co(II) species (Fig. 3). Based upon fundamental coordination chemistry principles, high-spin Co(II) is a labile metal that will undergo rapid ligand substitution reactions to form the most thermodynamically-favourable complex. Importantly the ligand field electronic structure extracted from the Co-bound CfbA MCD data strongly suggests that Ni-bound CfbA will have an octahedral, high-spin Ni(II) ion. Octahedral, high-spin Ni(II) is also labile, whereas a square planar Ni(II) ion would be low-spin and kinetically inert. Interestingly, previous studies have shown that the metal substrate of ferrochelatase is high-spin Fe(II).[54, 60] Thus, ferrochelatase also appears to exert important control over the coordination geometry and oxidation state of its metal substrate, iron, since high-spin Fe(II) is labile, but low-spin Fe(III) and Fe(II) are inert. As discussed in the final section, the observation that class II chelatases bind labile metal substrates has important implications for their enzymatic mechanism.

CfbA ruffles its tetrapyrrole substrate

Analysis of the UV/Vis Abs data presented here within the framework of DFT calculations strongly suggests that CfbA induces a ruffling out-of-plane distortion of its tetrapyrrole substrate in contrast to the saddling deformation reported for ferrochelatase. CfbA binding triggers a 300-400 cm^{-1} red-shift of the uroporphyrin and PPIX Soret bands (Fig. 4 and Table 1). DFT calculations have demonstrated that this is consistent with increased tetrapyrrole ruffling, but not saddling or deprotonation (Figs. 6-7). The choice of ruffling as an out-of-plane distortion by CfbA may have important implications for its native function as a nickel chelatase. Ruffled nickel tetrapyrroles are known to have an additional bonding interaction between the Ni $3d_{xy}$ and porphyrin a_{2u} orbitals,[59] which means that ruffling of a tetrapyrrole substrate may stabilize a nickel tetrapyrrole product and thermodynamically drive the reaction to completion. On the other hand, ferrochelatase has been shown to saddle its tetrapyrrole substrate.[54, 56] The saddling out-of-plane deformation drives the pyrrole nitrogen lone pairs out of the macrocyclic plane, which

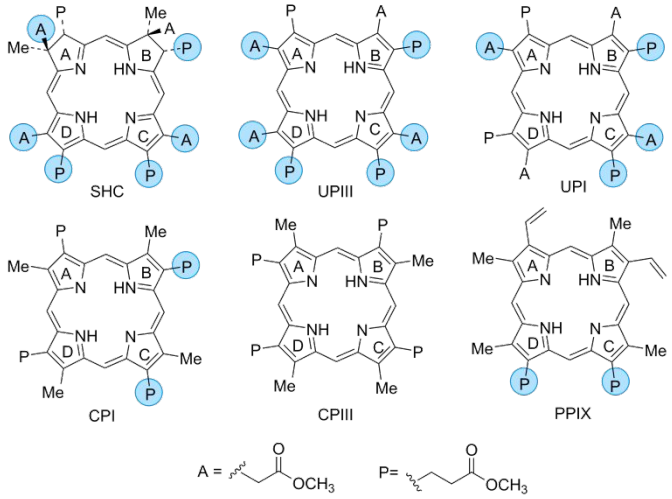

Fig. 8 Side-chain substitutions influence the degree of porphyrin out-of-plane deformation upon binding to CfbA and the rate enhancement for Co insertion. The side-chains highlighted in blue are identical to those of the native substrate, sirohydrochlorin (SHC).

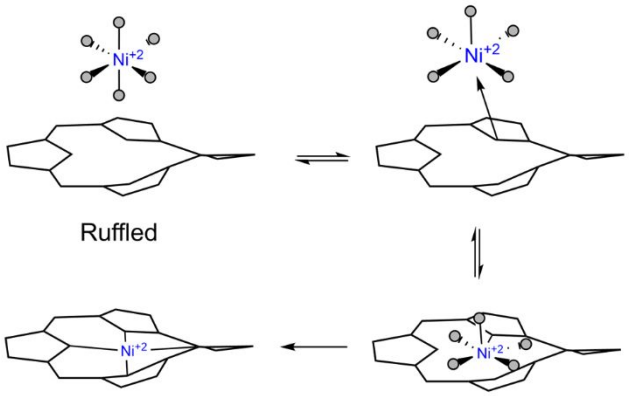

Fig. 9 Proposed mechanism for Ni(II) insertion into SHC by CfbA based upon the data presented in this article. Upon binding to CfbA, high-spin octahedral Ni(II) is labile and a rapid equilibrium will be established between six- and five-coordinate Ni(II). This strongly suggests that CfbA follows a dissociative substitution mechanism in order to insert Ni(II) into a ruffled SHC substrate.

is proposed to promote iron chelation.[61] Ruffling does *not* drive the pyrrole nitrogen lone pairs out of the macrocyclic plane,[42] and we will discuss the potential mechanistic implications of this deformation in the final section.

The ruffling deformation induced by CfbA depends upon the identity and isomer of the tetrapyrrole substrate. The UV/Vis Abs spectral changes observed upon binding coproporphryins to CfbA are inconsistent with deprotonation, saddling, or ruffling of these tetrapyrroles. The spectral data suggest that coproporphyrins are strongly perturbed upon binding to CfbA, but may not be properly positioned within the enzyme active site. On the other hand, uroporphyrins and PPIX exhibit moderately red-shifted Soret bands upon binding to CfbA, which is consistent with ruffling of these substrates. A closer examination of the data for the uroporphyrin isomers reveals that the magnitude of the ruffling deformation depends upon the exact pattern of side-chains around the tetrapyrrole core (Fig. 8). Uroporphyrin III, which has the same distribution of carboxylic acid side-chains as the native SHC substrate, is more ruffled than UPI. This strongly suggests that CfbA triggers a ruffling deformation of its native SHC substrate. With these details regarding nickel and SHC binding by CfbA now available, a mechanistic proposal emerges that has similarities to and differences from that of ferrochelatase.

The novel mechanism of CfbA is an ideal starting point for development of synthetic chelatases

The spectroscopic and computational data presented in this manuscript reveals that the mechanism of metal insertion by CfbA is distinct from that of ferrochelatase. Based upon the spectroscopic data presented here, and analysis of data available in the literature,[54, 60] both CfbA and ferrochelatase bind a labile metal. This means that the metal substrates of these enzymes will rapidly exchange ligands within the enzyme active sites and there is no kinetic barrier associated with metal desolvation. A major difference between CfbA and ferrochelatase is the manner in which these enzymes bind a tetrapyrrole substrate. Whereas ferrochelatase binds a saddled PPIX substrate,[54, 56] the spectroscopic and computational data presented here strongly suggests that CfbA binds a ruffled SHC substrate (Fig. 7). PPIX saddling is a key component of the proposed ferrochelatase mechanism since this out-of-plane distortion drives the pyrrole nitrogen lone pairs out of the macrocyclic plane and minimizes the kinetic barrier to iron–nitrogen bond formation.[61] The ruffling deformation induced by CfbA does *not* push the pyrrole nitrogen lone pairs out-of-plane, [42] so this enzyme must follow a unique mechanism. For CfbA, pushing the pyrrole nitrogen lone pairs out-of-plane may simply be unnecessary due to the smaller ionic radius of Ni(II). Instead, the ruffling deformation may offer a thermodynamic driving force for tetrapyrrole metalation by destabilizing the organic reactant and stabilizing the inorganic product (Fig. 9).[59]

It is worth noting that the data presented in this manuscript suggests that CfbA preferentially inserts nickel into its native tetrapyrrole substrate, SHC. Of the five tetrapyrrole substrates investigated in this work, SHC is most similar to UPIII (Fig. 8). SHC and UPIII have the same distribution of carboxylic acid side-chains, but pyrrole rings A and B are further reduced in SHC. UPIII is tied with PPIX as the most ruffled CfbA substrate investigated here (Table 1). Importantly, the UPIII analogue of SHC is more ruffled than UPI. Finally, CfbA-catalyzed nickel insertion is six-times faster than nickel insertion into UPI (Table 3). This is a striking reversal of tetrapyrrole substrate preference compared to cobalt insertion (Table 2). More definitive conclusions regarding the preference of CfbA for SHC will require future studies employing SHC itself, but these data identify an intriguing correlation between the identities of the tetrapyrrole side-chains and nickel insertion activity.

The mechanism of CfbA merits further investigation since this is the first enzyme shown to promote metal insertion into both porphyrins and bacteriochlorins. Previous studies have demonstrated that CfbA can insert Fe(II),[11, 19] Co(II),[11, 19, 20] and Ni(II)[11, 17, 21] into SHC based upon both *in vitro* and *in vivo* assays. Here, we have reported CfbA-promoted Co(II) insertion into

coproporphyrin, uroporphyrin, and PPIX based upon careful spectroscopic characterization of the reaction (Fig. 5). We have also observed CfbA-catalysed Ni(II) insertion into uroporphyrin. Co–PPIX is a particularly valuable product because this species has been shown to catalyse two reactions of particular relevance for the development of fuel cells.[62-69] Also, coproporphryin, uroporphyrin, PPIX, and SHC are a reasonably broad representation of tetrapyrrole structures and electronic structures. The number of propionate side-chains in this set of substrates ranges from two (PPIX) to eight (SHC), and the number of electrons in the tetrapyrrole π system ranges from 18 in SHC to 22 in the porphyrins. This broad substrate scope means that CfbA is a good starting point for design of synthetic chelatases via iterative improvement of existing function. The mechanistic insights revealed by this study represent a critical first step in this process.

Conclusions

In summary, this work has shown that CfbA has the broadest substrate scope of all characterized chelatases and has provided critical insight into the enzymatic mechanism. The metal binding site of CfbA accommodates an octahedral, high-spin Co(II) ion. Thus, the metal substrate is labile, metal desolvation is facile, and this is not the rate-limiting step of the reaction. The tetrapyrrole binding site of CfbA induces a ruffling deformation of this substrate. This ruffling distorition is distinct from the critical saddling deformation observed in ferrochelatase,[54, 56] which means that the CfbA mechanism must be different from that proposed for ferrochelatase.[61] These data reveal a fascinating correlation between native metal substrate identity and tetrapyrrole distortion.

Conflicts of interest

There are no conflicts to declare.

Acknowledgements

M.D.L. thanks the *University of Vermont* and the *National Science Foundation* (DMR-1506248) for financial support. A.A.S. thanks *St. Lawrence University* for financial support. The authors thank Andrea Lee (*University of Vermont*) for assistance with cloning, Alexis Haley (*St. Lawrence University*), and Bruce O'Rourke (*University of Vermont*) for assistance with ESI-MS data acquisition.

References

1 T. L. Poulos, *Chem. Rev.*, 2014, **114**, 3919-3962.
2 P. R. Ortiz de Montellano, *Cytochrome P450: Structure, Mechanism, and Biochemistry*, Springer International Publishing, Switzerland, 2015.
3 E. Raven and B. Dunford, *Heme Peroxidases*, Royal Society of Chemistry, Cambridge, UK, 2016.
4 S. Yoshikawa and A. Shimada, *Chem. Rev.*, 2015, **115**, 1936-1989.
5 R. G. Matthews, M. Koutmos and S. Datta, *Curr. Opin. Struct. Biol.*, 2008, **18**, 658-666.
6 R. Banerjee, *Chem. Rev.*, 2003, **103**, 2083-2094.
7 R. K. Thauer, *Biochemistry*, 2019, ASAP.
8 W. Zhang, W. Lai and R. Cao, *Chem. Rev.*, 2017, **117**, 3717-3797.
9 T. J. Lawton and A. C. Rosenzweig, *J. Am. Chem. Soc.*, 2016, **138**, 9327-9340.
10 D. Osman, M. A. Martini, A. W. Foster, J. Chen, A. J. P. Scott, R. J. Morton, J. W. Steed, E. Lurie-Luke, T. G. Huggins, A. D. Lawrence, E. Deery, M. J. Warren, P. T. Chivers and N. J. Robinson, *Nat. Chem. Biol.*, 2019, **15**, 241-249.
11 A. A. Brindley, E. Raux, H. K. Leech, H. L. Schubert and M. J. Warren, *J. Biol. Chem.*, 2003, **278**, 22388-22395.
12 M. Hansson, J. Lundqvist, N. Sirijovski and S. Al-Karadaghi, in *Handbook of Porphyrin Science: with applications to chemistry, physics, materials science, engineering, biology, and medicine*, eds. G. C. Ferreira, K. M. Kadish, K. M. Smith and R. Guilard, World Scientific, Hackensack, NJ, USA, 2013, vol. 28: chlorophyll, photosynthesis and bio-inspired energy.
13 E. Deery, S. Schroeder, A. D. Lawrence, S. L. Taylor, A. Seyedarabi, J. Waterman, K. S. Wilson, D. Brown, M. A. Geeves, M. J. Howard, R. W. Pickersgill and M. J. Warren, *Nat. Chem. Biol.*, 2012, **8**, 933-940.
14 H. A. Dailey, T. A. Dailey, C.-K. Wu, A. E. Medlock, K.-F. Wang, J. P. Rose and B.-C. Wang, *Cell Mol. Life Sci.*, 2000, **57**, 1909-1926.
15 E. Raux, C. Thermes, P. Heathcote, A. Rambach and M. J. Warren, *J. Bacteriol.*, 1997, **179**, 3202-3212.
16 H. K. Leech, E. Raux-Deery, P. Heathcote and M. J. Warren, *Biochem. Soc. Trans.*, 2002, **30**.
17 K. Zheng, P. D. Ngo, V. L. Owens, X.-P. Yang and S. O. Mansoorabadi, *Science*, 2016, **354**, 339-342.
18 G. Layer and M. J. Warren, in *Handbook of Porphyrin Science: with applications to chemistry, physics, materials science, engineering, biology, and medicine*, eds. K. M. Kadish, K. M. Smith and R. Guilard, World Scientific, Hackensack, NJ, USA, 2012, vol. 19: biochemistry of tetrapyrroles (part II).
19 A. Pisarchik, R. Petri and C. Schmidt-Dannert, *Protein Eng. Des. Sel.*, 2007, **20**, 257-265.
20 J. Yin, L. X. Xu, M. M. Cherney, E. Raux-Deery, A. A. Bindley, A. Savchenko, J. R. Walker, M. E. Cuff, M. J. Warren and M. N. G. James, *J. Struct. Func. Genom.*, 2006, **7**, 37-50.
21 S. J. Moore, S. T. Sowa, C. Schuchardt, E. Deery, A. D. Lawrence, J. V. Ramos, S. Billig, C. Birkemeyer, P. T. Chivers, M. J. Howard, S. E. J. Rigby, G. Layer and M. J. Warren, *Nature*, 2017, **543**, 78-82.
22 C. V. Romão, D. Ladakis, S. A. L. Lobo, M. A. Carrondo, A. A. Brindley, E. Deery, P. M. Matias, R. W. Pickersgill, L. M. Saraiva and M. J. Warren, *Proc. Natl. Acad. Sci.*, 2011, **108**, 97-102.
23 R. Wu, E. P. Skaar, R. Zhang, G. Joachmiak, P. Gornicki, O. Schneewind and A. Joachmiak, *J. Biol. Chem.*, 2005, **280**, 2840-2846.
24 R. B. Kapust, J. Tözsér, J. D. Fox, D. E. Anderson, S. Cherry, T. D. Copeland and D. S. Waugh, *Protein Eng.*, 2001, **14**, 993-1000.
25 S. Nallamsetty, R. B. Kapust, J. Tözsér, S. Cherry, J. E. Tropea, T. D. Copeland and D. S. Waugh, *Protein Expr. Purif.*, 2004, **37**, 108-115.

26 L. Bogorad, *J. Biol. Chem.*, 1958, **233**, 501-509.
27 C. Rimington, *Biochem. J.*, 1960, **75**, 620-623.
28 R. Giovannetti and V. Bartocci, *J. Liq. Chromatogr. Relat. Technol.*, 1998, **21**, 2607-2617.
29 E. Kazutoshi and I. Shukuro, *Bull. Chem. Soc. Jpn.*, 1995, **68**, 3085-3090.
30 C. Jullian, J. E. Brunet, V. Thomas and D. M. Jameson, *Biochim. Biophys. Acta*, 1989, **997**, 206-210.
31 I. Barr, S. H. Weitz, T. Atkin, P. Hsu, M. Karayiorgou, J. A. Gogos, S. Weiss and F. Guo, *Chem. Biol.*, 2015, **22**, 793-802.
32 F. Neese, *Wiley Interdiscip. Rev.: Comput. Mol. Sci.*, 2012, **2**, 73-78.
33 A. D. Becke, *Phys. Rev. A*, 1988, **38**, 3098-3100.
34 C. Lee, W. Yang and R. G. Parr, *Phys. Rev. B*, 1988, **37**, 785-789.
35 A. D. Becke, *J. Chem. Phys.*, 1993, **98**, 5648-5652.
36 J. P. Perdew, K. Burke and M. Ernzerhof, *Phys. Rev. Lett.*, 1996, **77**, 3865-3868.
37 J. P. Perdew, M. Ernzerhof and K. Burke, *J. Chem. Phys.*, 1996, **105**, 9982-9985.
38 F. Weigend and R. Ahlrichs, *Phys. Chem. Chem. Phys.*, 2005, **7**, 3297-3305.
39 V. Barone and M. Cossi, *J. Phys. Chem. A*, 1998, **102**, 1995-2001.
40 A. Laaksonen, *J. Mol. Graphics*, 1992, **10**, 33-34.
41 D. L. Bergman, L. Laaksonen and A. Laaksonen, *J. Mol. Graphics*, 1997, **15**, 301-306.
42 W. Jentzen, X.-Z. Song and J. A. Shelnutt, *J. Phys. Chem. B*, 1997, **101**, 1684-1699.
43 A. B. Graves, M. T. Graves and M. D. Liptak, *J. Phys. Chem. B*, 2016, **120**, 3844-3853.
44 A. J. McCaffery, P. J. Stephens and P. N. Schatz, *Inorg. Chem.*, 1967, **6**, 1614-1625.
45 E. Decaneto, T. Vasilevskaya, Y. Kutin, H. Ogata, M. Grossman, I. Sagi, M. Havenith, W. Lubitz, W. Thiel and N. Cox, *Phys. Chem. Chem. Phys.*, 2017, **19**.
46 J. A. Larrabee, C. M. Alessi, E. T. Asiedu, J. O. Cook, K. R. Hoerning, L. J. Klingler, G. S. Okin, S. G. Santee and T. L. Volkert, *J. Am. Chem. Soc.*, 1997, **119**, 4182-4196.
47 F. Neese and E. I. Solomon, *Inorg. Chem.*, 1999, **38**, 1847-1865.
48 L. M. Scolaro, M. Castriciano, A. Romeo, S. Patané, E. Cefalí and M. Allegrini, *J. Phys. Chem. B*, 2002, **106**, 2453-2459.
49 M. Gouterman, *J. Chem. Phys.*, 1959, **30**, 1139-1161.
50 T. Hashimoto, Y.-K. Choe, H. Nakano and K. Hirao, *J. Phys. Chem. A*, 1999, **103**, 1894-1904.
51 D. Sundholm, *Phys. Chem. Chem. Phys.*, 2000, **2**, 2275-2281.
52 J. E. Falk, *Porphyrins and Metalloporphyrins*, Elsevier, Amsterdam, 1964.
53 D. T. Nam, Y. B. Ivanova, S. G. Puhovskaya, K. M.M. and S. A. Syrbu, *RSC Adv.*, 2015, **5**, 26125-26131.
54 Y. Lu, A. Sousa, R. Franco, A. Mangravita, G. C. Ferreira, I. Moura and J. A. Shelnutt, *Biochemistry*, 2002, **41**, 8253-8262.
55 Z. Shi, R. Franco, R. Haddad, J. A. Shelnutt and G. C. Ferreira, *Biochemistry*, 2006, **45**, 2904-2912.
56 A. E. Medlock, L. Swartz, T. A. Dailey, H. A. Dailey and W. N. Lanzilotta, *Proc. Natl. Acad. Sci.*, 2007, **104**, 1789-1793.
57 R. Franco, S. Al-Karadaghi and G. C. Ferreira, *J. Porphyrins Phthalocyanines*, 2011, **15**, 357-363.
58 A. K. Wertsching, A. S. Koch and S. G. DiMagno, *J. Am. Chem. Soc.*, 2001, **123**, 3932-3939.
59 H. Ryeng and A. Ghosh, *J. Am. Chem. Soc.*, 2002, **124**, 8099-8103.
60 R. Franco, J. J. G. Moura, I. Moura, S. G. Lloyd, B. H. Huynh, W. S. Forbes and G. C. Ferreira, *J. Biol. Chem.*, 1995, **270**, 26352-26357.
61 S. Al-Karadaghi, R. Franco, M. Hansson, J. A. Shelnutt, G. Isaya and G. C. Ferreira, *Trends Biochem. Sci.*, 2006, **31**, 135-142.
62 J. G. Kleingardner, B. Kandemir and K. L. Bren, *J. Am. Chem. Soc.*, 2014, **136**, 4-7.
63 B. Kandemir, S. Chakraborty, Y. X. Guo and K. L. Bren, *Inorg. Chem.*, 2016, **55**, 467-477.
64 D. J. Sommer, M. D. Vaughn and G. Ghirlanda, *Chem. Commun.*, 2014, **50**.
65 D. J. Sommer, M. D. Vaughn, B. C. Clark, J. Tomlin, A. Roy and G. Ghirlanda, *Biochim. Biophys. Acta*, 2016, **1857**, 598-603.
66 J. P. Collman, P. Denisevich, Y. Konai, M. Marrocco, C. Koval and F. C. Anson, *J. Am. Chem. Soc.*, 1980, **102**, 6027-6036.
67 R. R. Durand, C. S. Bencosme, J. P. Collman and F. C. Anson, *J. Am. Chem. Soc.*, 1983, **105**, 2710-2718.
68 Y. L. Mest, C. Inisan, A. Laouenan, M. L'Her, J. Talarmin, E. M. Khalifa and J.-Y. Sailard, *J. Am. Chem. Soc.*, 1997, **119**, 6095-6106.
69 C. J. Chang, Y. Deng, C. Shi, C. K. Chang, F. C. Anson and D. G. Nocera, *Chem. Commun.*, 2000, **15**, 1355-1356.

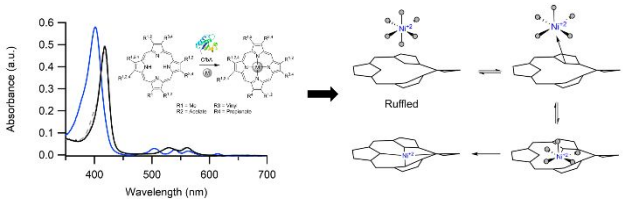

TOC Figure. CfbA inserts a labile metal into a ruffled tetrapyrrole